



HAL
open science

Observing the subglacial hydrology network and its dynamics with a dense seismic array

Ugo Nanni, Florent Gimbert, Philippe Roux, Albanne Lecointre

► To cite this version:

Ugo Nanni, Florent Gimbert, Philippe Roux, Albanne Lecointre. Observing the subglacial hydrology network and its dynamics with a dense seismic array. Proceedings of the National Academy of Sciences of the United States of America, 2021, 118, 10.1073/pnas.2023757118 . insu-03594399

HAL Id: insu-03594399

<https://insu.hal.science/insu-03594399>

Submitted on 5 Apr 2024

HAL is a multi-disciplinary open access archive for the deposit and dissemination of scientific research documents, whether they are published or not. The documents may come from teaching and research institutions in France or abroad, or from public or private research centers.

L'archive ouverte pluridisciplinaire **HAL**, est destinée au dépôt et à la diffusion de documents scientifiques de niveau recherche, publiés ou non, émanant des établissements d'enseignement et de recherche français ou étrangers, des laboratoires publics ou privés.

PNAS

www.pnas.org

1

2 **Main Manuscript for**

3 Observing the subglacial hydrology network and its dynamics with a
4 dense seismic array

5 Ugo Nanni¹, Florent Gimbert¹, Philippe Roux² and Albanne Lecointre²

6 ¹, IGE, Univ. Grenoble Alpes, CNRS, IRD, Grenoble, France

7 ², ISTERre, Univ. Grenoble Alpes, Univ. Savoie Mont Blanc, CNRS, IRD, IFSTTAR, Grenoble,
8 France

9 * Ugo Nanni

10 **Email:** ugo.nanni@univ-grenoble-alpes.fr

11 **Author Contributions:**

12 U.N., F.G., P.R. designed the study; U.N., F.G., P.R. participated in the field installations; U.N.,
13 F.G., P.R., A.L. performed the research; U.N., F.G., P.R., A.L. analyzed the data; U.N. wrote the
14 paper with help from F.G. and P.R.

15 **Competing Interest Statement:**

16 The authors declare that they have no competing financial interests

17 **Classification:**

18 Physical Sciences - Earth, Atmospheric, and Planetary Sciences

19 **Keywords:**

20 Cryoseismology – Subglacial hydrology – dense seismic array – seismic noise sources

21 **This PDF file includes:**

22 Main Text

23 Figures 1 to 4

24 **Abstract**

25 Subglacial water flow strongly modulates glacier basal motion, which itself strongly influences the
26 contributions of glaciers and ice sheets to sea-level rise. However, our understanding of when and
27 where subglacial water flow enhances or impedes glacier flow is limited due to the paucity of direct
28 observations of subglacial drainage characteristics. Here we demonstrate that dense seismic array
29 observations combined with an innovative systematic seismic source location technique allows for
30 the first time the retrieval of a two-dimensional map of a subglacial drainage system, as well as its
31 day-to-day temporal evolution. We observe with unprecedented detail when and where subglacial
32 water flows through a cavity-like system that enhances glacier flow versus when and where water
33 mainly flows through a channel-like system that impedes glacier flow. Most importantly, we are
34 able to identify regions of high hydraulic connectivity within and across the cavity and channel
35 systems, which have been identified as having a major impact on the long term glacier response
36 to climate warming. Applying a similar seismic monitoring strategy in other glacier settings,
37 including for ice sheets, may help to diagnose the susceptibility of their dynamics to increased
38 meltwater input due to climate warming.

39 **Significance Statement**

40 Our understanding of when, where and under which conditions subglacial water flow favors or
41 impedes glacier flow remains uncertain mainly because of sparse field observations. This strongly
42 limits our capability to assess the susceptibility of glaciers and ice-sheets to a future increase in
43 meltwater input due to climate warming. Here we overcome classic observational difficulties by
44 establishing an innovative seismic-based approach. From dense-seismic array observations we
45 retrieve with unprecedented detail the two-dimensional map of a subglacial hydrology network.
46 We observe its day-to-day evolution from a cavity-dominated system that favors glacier flow to a
47 channel-dominated system that impedes glacier flow. Although our method was applied on an
48 Alpine Glacier, it is easily adaptable and readily applicable to other settings such as Greenland or
49 Antarctica.

50

51 **Main Text**

52

53 **Introduction**

54

55 Meltwater produced at the surface of a glacier is mostly routed to its bed through crevasses and
56 moulins and flows towards its terminus through the subglacial drainage system¹. In this system,
57 water pressure regulates the ice–bed mechanical coupling, which determines the glacier sliding
58 speed, and therefore has major effects on the stability of glaciers and ice sheets^{2,3} and their
59 contributions to sea-level rise^{4–6}. Subglacial water pressure shows complex dependency on the
60 subglacial route that the water follows, and in particular on whether the water flows through a
61 distributed and inefficient system⁷ (e.g. cavity-dominated for hard bed glaciers) or a localized and
62 efficient system⁸ (channel-dominated drainage system is expected to be associated with a,
63 comparatively, lower water pressure, which promotes low glacier sliding speeds^{8,10–12}. Where
64 cavities are hydraulically well connected to channels they drain into the efficient drainage
65 system, which tends to lower the overall water pressure¹³. In addition, recent observations¹³

66 suggested that hydraulically isolated areas of the bed with very low permeability¹⁵ regulate glacier
67 basal traction during winter¹⁶ and over multi-annual timescales¹⁷. The spatial persistence of high
68 water pressure at the glacier bed¹⁴ thus depends on the subglacial drainage system configuration
69 and the hydraulic connectivity across the cavities and from the cavities to the channels. However,
70 current observations of subglacial drainage systems are rather point-scale^{14,18} (e.g., via ice-
71 drilling) or spatially-integrated^{19,20} (e.g. via dye tracing experiments or hydrochemical analysis),
72 such that they provide only partial representations of the heterogeneous nature of the subglacial
73 drainage system. It thus remains uncertain where and when isolated cavities, connected cavities,
74 and/or channels operate, and therefore under what conditions (e.g., water supply rate, glacier
75 geometry) meltwater supply to the glacial bed enhances or limits glacier flow.

76 Recent studies have indicated that turbulent subglacial water flow generates detectable seismic
77 noise²¹ given flow velocities of the order of a meter per second²², that can be used to retrieve the
78 physical properties of subglacial channels (e.g., water pressure, conduit size)^{22,23} as well as to
79 estimate their location in space^{24,25}. Previous studies that have attempted to spatially track water
80 flow have documented their azimuthal distribution, but not their epicentral coordinates^{24–26}.

81 Location of epicentral coordinates of simultaneously active and spatially spread noise sources
82 indeed represents a major seismological challenge²⁷, since it requires observations of the
83 wavefield all around the targeted sources with high enough resolution to deal with its strong
84 incoherency^{28,29}. Here, we demonstrate that well-resolved maps of subglacial drainage systems
85 can be retrieved using particularly dense seismic arrays and by adapting the matched-field
86 processing (MFP) technique²⁸ to the particularity of dealing with spatially spread sources.

87 **Seismic monitoring and source location strategy**

88 We use the 1-month seismic record from 98 three-component sensors that was acquired at the
89 surface of glacier d'Argentière (French Alps; Fig. 1) during the onset of the 2018 melt-season
90 (see Methods and ref.³⁰ for detailed description of the experiment and ref.²³ for a broader
91 glaciological context). At this location, subglacial water flow strongly influences glacier dynamics³¹

92 and generates continuous seismic noise that is most pronounced in the [3-7] Hz frequency
93 range²³, in which seismic wavelengths are on the order of [200-500] m³². Our seismic array
94 covers an area of 400 x 600 m² with a 40-m to 50-m sensor spacing and an aperture (i.e. largest
95 distance between stations; Fig. 1) of ca. 720m. Such configuration allows subwavelength
96 sampling while covering all azimuthal directions around the targeted sources, which are two
97 necessary conditions for retrieving the epicentral coordinates of seismic sources through
98 application of MFP^{28,29}(Methods). MFP consists of recursively matching the predicted and
99 observed phase delays (Methods), and has been extensively applied to locate spatially well-
100 separated sources, such as those generated by hydrothermal activity³³, oil and gas injection³⁴,
101 icequakes³², or englacial moulines³². However, it has been little applied to locate spatially
102 distributed noise sources^{34,35}. We adapt this technique to provide such particularity through a
103 systematic analysis of the phase coherence over 1-s-long time windows. Within each window, we
104 apply an efficient gradient-based minimization algorithm that allows us to locate up to 29
105 simultaneously active sources (Methods). We obtain each source location from maximizing the
106 correlation between the observed and the modeled phase delays. We refer to this maximum
107 correlation as the MFP output, which ranges from 0 to 1. An MFP output close to 1 indicates
108 global phase coherence, as expected for a dominant and punctual source³⁶, while a low MFP
109 output indicates several local phase coherences, as expected for multiple sources simultaneously
110 acting over the area. We note that we only keep the sources that are located within 400 m of the
111 center of our array and are associated with realistic physical properties (i.e., wave velocities,
112 source depth; Fig. 2b, c). This yields more than a million seismic sources per day (Fig. 2a).

113 **Retrieving the geometry of the subglacial system**

114 In Figure 2d, e, we show the normalized spatial distribution probability of the source location
115 obtained over the study period for high and low MFP output ranges, as indicated in Figure 2a. We
116 observe that events associated with high (i.e., global) phase coherence (MFP output, >0.8) are
117 mainly located at the glacier surface (Fig. 2b) where crevasses are observed (Fig. 2e), and are

118 associated with phase velocities that are typical of surface waves³⁷ (ca. 1580 m.s⁻¹; Fig. 2c). This
119 is consistent with these events corresponding to crevasse-induced icequakes (Fig. 1). On the
120 contrary, sources associated with low (i.e., local) phase coherence (MFP output, [0.05-0.3]) are
121 preferentially located at depth near the ice–bed interface (Fig. 2b). The associated phase
122 velocities (Fig. 2c) vary by up to ca. 3600 m.s⁻¹, which is consistent with body waves being
123 generated additionally to surface waves, and thus with sources that occur at depth³⁸. The spatial
124 distribution of these sources show two elongated regions located along the glacier centerline (one
125 at maximum ice thickness and one 50 m further down-glacier) where hydraulic potential
126 calculations allow materializing the likely location of subglacial channel(s) (Fig. 2d; see Methods
127 for details on the hydraulic potential calculations). All of these concomitant features lead us to
128 interpret these observed seismic sources as a depiction of the geometry of the subglacial
129 drainage system. The characteristic width of the observed spots (ca. 50 m, Fig. 2d) is much
130 greater than might be expected for a single subglacial channel (on the order of meter to few
131 meters⁸), which could result from the location resolution being limited by the seismic wavelength
132 investigated (expected to be 1/6 to 1/2 times the ca. 300m wavelength; see Methods) or from the
133 presence of multiple channels. The absence of clear source locations in the up-glacier part of the
134 array (Fig. 3) might be caused by reduced or less turbulent subglacial water flow there, compared
135 to the down-glacier part, where over-deepening of the glacier bed might favor unstable and more
136 turbulent water flow³⁹.

137

138 **Observing the switch from a cavity-like to a channel-like drainage system**

139 We further investigate whether with our observational technique we can retrieve the different
140 components of a subglacial drainage system by evaluating temporal changes in the source
141 location maps together with the subglacial flow parameters that characterize average water
142 drainage efficiency and water pressure conditions at the glacier bed^{22,23} (see Methods for details).
143 We calculate source location maps averaged over 2-day time windows (Fig. 3) and use the

144 combined seismic signal amplitude and water discharge measurements to invert for spatially-
145 integrated changes in the hydraulic pressure gradient and hydraulic radius of the subglacial
146 drainage system (Fig. 4)^{22,23}. All maps are obtained from sources yielding a similar phase
147 coherence (i.e. associated with MFP output within the same narrow [0.07-0.16] range) such that
148 they are retrieved with a similar accuracy (see Methods).

149 We observe that sources are spatially more distributed at the beginning of the period (until ca.
150 May 10; Fig. 3) than when averaging source locations over the whole period (Fig. 2d). At this time
151 the hydraulic pressure gradient (Fig. 4a, green line) varies significantly with the discharge (from
152 $0.1 \text{ m}^3 \cdot \text{s}^{-1}$ to $2 \text{ m}^3 \cdot \text{s}^{-1}$; Fig. 4b, blue line) and the hydraulic radius remains constant (Fig. 4a, purple
153 line), which indicates low drainage efficiency²³. This time period is also associated with marked
154 glacier surface acceleration (velocity increases by up to ca. 50%) due to enhanced basal sliding³¹
155 as a result of the subglacial water pressurization⁷. These concomitant observations provide
156 strong support that with our source location analysis we can observe water flow in the cavity-like
157 system. This has not been suggested in previous cryoseismic studies^{21–23,25} on the premise that
158 fast and turbulent water flow speeds (as $\text{m} \cdot \text{s}^{-1}$; i.e., seismically detectable²²) only occur in
159 channels. However this is consistent with borehole field observations^{14,40} and with theoretical
160 studies that have envisioned channel-like flow in connections between cavities (referred to as
161 orifices)⁹.

162 While progressing through time (from ca. May 10), the subglacial water flow localizes into a
163 narrower zone (Fig. 3). This transition towards a channel-dominated system is well revealed by
164 the significant increase in the two-dimensional coefficient of determination R^2 (Fig. 4a) calculated
165 between the spatial pattern observed for May 25-26 (Fig. 3o) and each of the patterns shown in
166 Figure 3. Concomitantly, and in contrast to the first part of the period, we observe a doubling of
167 the hydraulic radius with a reduced and almost unvarying hydraulic pressure gradient, which
168 indicates that the increasing drainage efficiency lowers the basal water pressure. Such an
169 increase in drainage efficiency is consistent with the increase in water discharge not resulting in

170 glacier acceleration, but rather in slight deceleration⁴¹. Our seismic analysis therefore provides
171 independent observational support for the hypothesis that the development of an efficient and
172 channel-like system reduces the basal water pressure and favors slower glacier flow.

173

174 **Implications for the monitoring of hydraulic connectivity within and across subglacial** 175 **drainage systems**

176 The presence of seismically detectable turbulent water flow within the cavity-like drainage system
177 suggests that this system is, at least in certain places, associated with high hydraulic connectivity.

178 The absence of seismic sources over many areas of the glacier bed indicates that these,
179 comparatively, have lower hydraulic connectivity, and could correspond to hydraulically isolated
180 portions of the bed with higher potential for water storage^{13,15}. This shows not only that our
181 seismic analysis can determine when and where the transition from a cavity-like to a channel-like
182 system occurs, but also that it can identify locations with high hydraulic connectivity within the
183 cavity-like system and from the cavity- to the channel-like systems. This implies that we can
184 evaluate which areas of the glacier bed are efficiently connected to channels, and thus drained
185 when they develop, versus the areas where water is stored and is thought to regulate the basal
186 traction over multi-year timescales^{15,17}. Yielding such observations in other settings like
187 Greenland has the potential for identifying locations where ice dynamics are expected to be
188 particularly sensitive to the foreseen increase in melt water input rates due to climate warming³.

189 **Perspectives and limitations**

190 A successful application of our methodology to other glacier systems like Ice-Sheet outlet glaciers
191 relies on the capability to conduct subwavelength sampling over representative areas (Methods),
192 ranging from about 1x1km² (e.g. Russel Glacier's tongue⁴²) up to about 10x10km² (e.g. central
193 trunk of Pine Island Glacier⁴³). These scaling constraints can be can be fulfilled through deploying
194 c. 100 up to c. 10,000 sensors in these areas, which we foresee as achievable in the near future
195 given the recent ease of dense seismic array installations in remote areas⁴⁴⁻⁴⁶.

196 Although the present seismic approach yields unprecedented insights on subglacial hydrology from
197 the local (Fig. 3) up to the glacier (Fig. 4) scales, future applications will likely still strongly benefit
198 from combination with complementary in-situ observations. Such a combination will guide the
199 strategy for conducting local (e.g., via ice-drilling) or spatially-integrated (e.g. via dye tracing
200 experiments or hydrochemical analysis) measurements in targeted and representative places
201 identified from the seismic observations. Complementary measurements in those targeted places
202 will also help enhance the level of quantitative interpretation of seismic observations through
203 giving more quantitative constraints on the behavior of key physical variables (pressure, flow
204 speed, connectivity) in each identified subglacial hydrology system. This integrated strategy will
205 allow to better extrapolate physical constraints from the local up to the glacier-wide scale, which
206 will ultimately facilitate the assimilation of seismic observations in subglacial hydrology – ice
207 dynamics coupled models, which otherwise remain poorly constrained across scales⁴⁷.

208 **Conclusion**

209 In this study, we provide well-resolved spatial observations of a localized efficient channel-like
210 system geometry and of the extent of a distributed inefficient cavity-like system. We show that
211 with an adapted systematic seismic investigation of low spatial phase coherences we can locate
212 multiple seismic noise sources induced by subglacial water flow that act at the same time. This
213 location procedure is feasible from very low water discharge ($\sim 0.1 \text{ m}^3 \cdot \text{s}^{-1}$) to peak melt-season
214 water discharge. Thus, we can simultaneously observe the distributed and localized drainage
215 systems through time and space, and evaluate the hydraulic connectivity within and across these
216 systems along with their changes through time. Our geophysical approach is also exportable to
217 other glaciers in remote areas, from mountain glaciers to ice caps, especially with the current
218 easing of dense-seismic arrays⁴⁶ and distributed acoustic sensing^{44,48} deployments. Our novel
219 way of investigating subglacial drainage systems will allow the glaciological community to
220 diagnose the susceptibility of ice sheets^{15,17} and mountain glaciers^{14,47} to increased meltwater
221 input due to climate warming and/or extreme melt and rainfall events. Our approach will also be

222 particularly appropriate to study processes that generate similar spatially spread seismic noise in
223 other environments, such as for lava flows on volcanoes⁴⁹, tremors in fault zones⁵⁰, and sediment
224 transport in rivers⁵¹.

225

226 **Materials and Methods**

227

228 *Dense seismic array survey*

229 All of the stations have a 500-Hz sampling rate and a low cut-off frequency of 4.5 Hz. The nodes
230 were installed at a depth of 30 cm into the 4-m-thick snow cover, and had to be reinstalled on
231 May 11 due to snow melt, which occurred at a rate of 5 cm.day⁻¹. We refer the reader to ref.³⁰ for
232 the detailed description of the experiment.

233 *Complementary measurements*

234 Concomitant with our seismic survey, we use continuous records of subglacial water discharge,
235 which was measured in excavated subglacial tunnels maintained by the hydroelectric power
236 company Emosson S.A. at ca. 600 m downstream of the center of the node-array (at 2173 m
237 a.s.l.). We also installed four GNSS stations at the corners of the seismic array to measure glacial
238 surface velocity, which was on the order of 0.1 m.day⁻¹ at this time of the year and for this part of
239 the glacier³¹. One week prior to the seismic deployment, we conducted a ground penetrating
240 radar campaign over the study area with a 5-MHz signal, to improve the previous estimates of the
241 bed topography reported by ref. ⁵². Also, in September 2018, we conducted an aerial survey to
242 derive a digital elevation model of the glacier surface using stereo-photogrammetry. Combining
243 these two digital elevation models, we calculated the ice thickness distribution over the study
244 area, as shown in Figure 1. The ice thickness reached up to 270 m at the center of the seismic
245 array, with a well-marked talweg (i.e., valley-shaped bed) aligned in the glacier flow direction, and
246 a progressive diminution of the ice thickness down-glacier both within the area covered by our
247 array and from the location of our array towards the glacier terminus. The reader should refer to

248 ref.³⁰ for the detailed description of the complementary data associated with this seismic
249 experiment.

250 *Matched field processing*

251 Matched field processing (MFP) consists of providing a probabilistic estimate of the epicentral
252 coordinate of dominant source²⁸ from evaluation of the phase coherence of the seismic signal
253 over an array of sensors. The method consists of recursively matching the phase delays of a
254 model-based synthetic wave-field (i.e., the ‘trial source’) with the phase delays observed between
255 the sensors over the array. A condition for this method to be applicable is that spatially coherent
256 phase information can be extracted between nearby sensors²⁸, which requires interstation
257 spacing of less than one-half of the investigated wavelength. We satisfy this conditions with our
258 40 to 50 m interstation spacing for a 200 to 500m investigated wavelength.

259 We first compute the discrete Fourier transform of a given data vector $d(t)$ recorded by the 98
260 sensors over a frequency ω , to obtain the complex data vector $d(\omega)$ and to calculate the
261 corresponding cross-spectral density matrix as

$$262 \quad K(\omega) = d(\omega)d^H(\omega),$$

263 where H is the Hermitian transpose. The cross-spectral density matrix captures the relative
264 spatial phase difference between the sensors. We then define a set of values to be explored for
265 trial sources. In this study, we set four degrees of freedom for the MFP processing, with a depth,
266 range and phase velocity grid (X, Y, Z, C). An important condition for retrieving source epicentral
267 coordinate (i.e. X, Y, Z) and not only source back azimuth is to have a source-to-array distance
268 not greater than two to three times the array aperture (i.e. largest distance between stations)²⁹.
269 We satisfy this condition with a c. 750 m array aperture for a c. 270m source-to-station
270 distances²³ (i.e. maximum glacier thickness⁵³). For each element a of these four dimensions of
271 the grid we model the Green’s function replica vector $d(\omega, a)$ under the hypothesis of a
272 homogenous medium as

273

$$d(\omega, a) = \exp\left(i\omega r_a/c\right),$$

274

where c is the medium velocity and r_a is the distance between each receiver and the trial source

275

position a .

276

To match the observed cross-spectral density matrix with the replica vector, we calculate the

277

Bartlett processor as

278

$$B_{Bartlett}(\omega, a) = \sum_{\omega} |d(\omega, a)^H K(\omega) d(\omega, a)|.$$

279

This operation is equivalent to cross-correlation between the observed wave-field phase and the

280

modeled one. We refer to the $B_{Bartlett}(\omega)$ values as the MFP output. The MFP output is

281

calculated at specific frequencies, and ranges from 0 to 1. The closer to 1 the MFP output is, the

282

more the modeled phase matches the observations. Sources that generate a signal resulting in

283

similar phase coherence (i.e. MFP output value) are expected to be localized with a similar

284

accuracy²⁸.

285

We perform source location over 1-s-long signal segments of the vertical component only. We

286

filter the signal within the [3-7] Hz frequency range that is the most sensitive to subglacial water

287

flow induced seismic noise^{21,23-25}, and coherently apply the MFP for each 0.4 Hz within this

288

range. To maximize the efficiency of our algorithm and minimize the computational costs, we use

289

a gradient-based minimization algorithm (i.e., Nelder-Mead optimization⁵⁴) to converge to the best

290

match between the trial and the observed phase delays, rather than exhaustive grid-search

291

exploration. The convergence criterion is reached when the variance of the values obtained over

292

the last five iterations of the optimization is $<1e^{-2}$, with a maximum of 3000 iterations. Our 29

293

different starting points used for optimization are located 250 m below the glacier surface, and

294

they uniformly cover an area of $800 \times 800 \text{ m}^2$ centered on the array (Fig. 2d). We set the initial

295

velocity to $1800 \text{ m}\cdot\text{s}^{-1}$. The 29 point locations found per signal segment (1 s) after convergence

296

are all located in the same place if clear global convergence exists (i.e., high MFP output) or at up

297 to 29 different locations if up to 29 local minima exist (i.e., low MFP output). The MFP output
298 value can also be understood as an indicator of the number of receivers over which the signal is
299 coherent; e.g., a value of 0.1 indicates a source that generates a signal coherent over 10% of the
300 array. We found that this approach is comparable to using sub-arrays of variable sizes to perform
301 the MFP over different areas of the glaciers. Further details on the methods and related physics
302 can be found in ref. ⁵⁵.

303 *Matched field processing output statistics*

304 We narrow the MFP output selection by keeping only: (1) the location that yields realistic phase
305 velocities ([1200-3600] m.s-1); and (2) the localizations at ± 400 m from the array center and ≤ 400
306 m below the glacier surface. The number of located sources after this selection (Fig. 2a)
307 decreases as the MFP output increases, with >5000 daily sources associated with MFP output
308 <0.05 , and <1 daily source associated with MFP output >0.75 . Figure 2b, c shows the distribution
309 of the source properties (vertical position), and Figure 2e, f shows the spatial probability of the
310 source location over the complete study period for two MFP output bands of ([0.07-0.16] and
311 [0.75-0.99]). These locations correspond to real and detectable seismic events, since MFP output
312 is much higher than expected for random noise (see ref.³⁰, [Fig. 9](#)). This two-dimensional
313 representation is obtained by summing the total number of sources in each 8×8 m² cell of an
314 800×800 m² (x, y) grid centered on our seismic array.

315 It is important to note that at low MFP output (e.g., [0.07-0.16]) only a few sensors distinguish the
316 source. This leads to a shorter aperture of the effective seismic array, which limits depth
317 resolution. The trend to higher probability of the source location at depth is however observed
318 here for tens of thousands of sources. The 2-day averaging is long enough to gather sufficient
319 statistics, while it is also short enough to correctly investigate the temporal evolution with high
320 enough spatial accuracy (Fig. 3).

321 *Source location precision*

322 When compared to the crevasse field at our study location (Fig. 1), we observe that our MFP
323 analysis yields source locations with MFP output >0.75 , a precision in range down to 10 m (Fig.
324 2) for an average wavelength λ of ca. 300 m at 5 Hz³⁷. While the expected Rayleigh limit gives
325 maximum resolution of $\lambda/4$ (ca. 75 m at 5 Hz) in the far-field domains²⁷, laboratory experiments⁵⁶
326 suggest that the seismic signal bears information of spatial structures down to $\lambda/8$ (ca. 32 m at 5
327 Hz) in the near-field of sources. Our unique instrumental set-up combined with our systematic
328 analysis of phase coherence allow us to overcome the Rayleigh far-field limitations and obtain
329 two-dimensional maps of source locations with resolution in the range of ca. 10 m for high MFP
330 outputs. For lower MFP outputs, we expect lower resolution due to the smaller aperture of the
331 array that is sensitive to local phase coherence. We acknowledge that the width of the area
332 shown in Figure 2d might not represent the true width of a single subglacial channel, which is
333 expected to be of the order of one to few meters at this location²³. The observed width of c. 50 m
334 could be due to the uncertainty for the source location or to the presence of multiple channels

335 *Hydraulic potential calculation*

336 We calculate the hydraulic potential Φ following ref.¹, as:

$$337 \quad \Phi = \rho_w g z_b + K[\rho_i g(z_s - z_b)],$$

338 where g is the acceleration due to gravity (9.81 m.s^{-2}), ρ_w is the density of water (1000 kg.m^{-3}), ρ_i
339 is the density of ice (917 kg.m^{-3}), z_b and z_s are the elevation of the glacier bed and surface (m),
340 respectively, and K is the ratio of water pressure to ice overburden pressure; i.e., a uniform
341 flotation fraction. A value of K near 0 represents a condition where basal water pressure is
342 negligible in comparison to ice overburden pressure, and a value near 1 represents a condition
343 where basal water pressure is high enough to significantly counterbalance ice overburden
344 pressure. Here we use a flotation fraction of 0.5, which is likely to represent a case where the
345 subglacial drainage system has developed enough to efficiently drain the bed^{1,57}, and therefore
346 reduce subglacial basal water pressure. We consider this flotation fraction to best represent the

347 subglacial water pressure condition in our location at the end of our study period when we
348 observe a decreasing glacier velocity while water discharge still increases (Fig. 4a). We then
349 calculate the water flow directions based on the hydraulic potential gradients, by following the
350 path that minimizes the gradient with a minimum upstream area of 150 m² for the waterway, to
351 initiate the use of TopoToolBox, developed by ref.⁵⁸. We show in Figure Supp. 1 that different
352 values of flotation fraction ($K = [0.1, 0.5, 0.9]$) result in a similar predicted waterway pattern. The
353 expected localization of subglacial water flow thus does not depend much on the flotation fraction,
354 likely as a result of the V-shape of the Argentière glacier being particularly pronounced.

355

356 *Inverting hydraulic properties using water discharge and seismic power measurements*

357 We use the theoretical framework of ref. ²² to invert for the hydraulic properties of subglacial
358 turbulent water flow using simultaneous measurements of subglacial water discharge and seismic
359 power. The seismic power P is calculated at each sensor using the vertical component of ground
360 motion within [3-7] Hz and the Welch method over 4-s time windows with 50% overlap, as
361 reported in ref. ²³. The physical framework relates the changes in the measured seismic power P
362 and discharge Q to changes in channel hydraulic radius R and hydraulic pressure gradient S . The
363 basis of these relations is that turbulence within water flow generates frictional forces that act on
364 the boundaries of the channels (i.e., ice, glacier bed) and create ground motion. This approach
365 has been recently shown to be applicable over our study area²³. The hydraulic radius R is defined
366 as the ratio of the cross-sectional area of the channel flow to its wetted perimeter. The hydraulic
367 pressure gradient S is a function of both the rate of change of water pressure and the bed slope
368 in the flow direction. In the case of constant bed slope and channel geometry, increasing S
369 means closed and pressurizing channel flow. Both variables are defined for subglacial conduits
370 where turbulent water flow dominates. We calculate median values of R and S using the median
371 seismic power P over the 98 sensors and the water discharge Q , as follows

372
$$S = S_{ref} \left(\frac{P}{P_{ref}} \right)^{24/41} \left(\frac{Q}{Q_{ef}} \right)^{-30/41},$$

373

374
$$R = R_{ref} \left(\frac{P}{P_{ref}} \right)^{-9/82} \left(\frac{Q}{Q_{ef}} \right)^{-33/82}$$

375 where the subset ref is the reference state, which is April 26 in this study. In the main text, when
376 referring to the temporal evolution of R and S, we therefore refer to their relative changes with
377 respect to this reference period. We evaluate P over the [3-7] Hz frequency band, as it has been
378 shown by ref. ²³ to be the best suited in area for studying turbulent water flow. The reader is
379 referred to refs. ^{22,23} for more details.

380 We stress that the inversions of hydraulic properties depend on the average seismic amplitude,
381 with very little dependency on the spatial variations. Therefore, our inversions are to be
382 considered independent of the source location, even if they both arise from the seismic signals.
383 This also implies that our inversions represent averaged hydraulic conditions of the drainage
384 system.

385 *State of knowledge on the main features of channels and cavities*

386 Cavities form in the downstream lee of bedrock bumps, due to ice sliding over the bed, and they
387 close through ice creep. Cavities can be filled with water, which reduces the apparent rugosity of
388 the glacier bed and weakens the ice–bed mechanical coupling³⁹. For soft-bed glaciers, inefficient
389 drainage systems also include unconsolidated layers of low permeability⁵⁹. Weakly connected
390 cavities can have permeability that are lower by ca. 9 orders of magnitude than that of connected
391 cavities¹⁵. For a similar hydraulic gradient to that of connected cavities, turbulent water flow within
392 a weakly connected system therefore requires much higher flow velocities.

393 Subglacial channels can be of the R-type⁸ when melted into the ice by turbulent dissipation of
394 heat, or of the N-type⁶⁰ when dug into the basal sediments by the flowing water or etched into

395 bedrock by carbonate dissolution⁶¹. Both types close through ice creep. When developing and
396 reaching steady-state, a subglacial channel tends to have lower water pressure than cavities,
397 which therefore drains the connected cavity system.

398

399

400

401 **Acknowledgments**

402

403 This work has been conducted in the framework of the RESOLVE Project (<https://resolve.osug.fr/>)
404 (LabEx OSUG@2020, Investissement d'avenir – ANR10LABX56 and IDEX Université Grenoble
405 Alpes). Most of the computations presented in this paper were performed using the GRICAD
406 infrastructure (<https://gricad.univ-grenoble-alpes.fr>), which is supported by Grenoble research
407 communities, and with the CiGri tool (<https://github.com/oar-team/cigri>) that was developed by
408 Gricad, Grid5000 (<https://www.grid5000.fr>) and LIG (<https://www.liglab.fr/>). FG acknowledges
409 support from ANR SEISMORIV (ANR-17-CE01-0008) and SAUSSURE (ANR-18-CE01-0015-01).

410 We thank Christian Vincent and Nathan Maier for feedback on paper writing and data
411 interpretation. We thank Agnès Helmstetter and Benoit Urruty for fruitful discussion on data
412 analysis. We thank Mondher Chekki for numerical support dealing with the dense seismic array
413 big dataset. U.N. thanks Aurélien Mordret, Amandine Sergeant, Léonard Seydoux, Jean
414 Soubestre, and Josefine Umlauf for discussions on locating spatially spread seismic noise
415 sources, and we thank Camillo Rada for discussions on subglacial drainage. U.N. thanks Pete
416 Akers, Jordi Bolibar, Fanny Brun, David Laliche, Fabien Moustard, Hans Segura and Jonathan
417 Wille for fruitful discussions on this work.

418 **Codes and data availability**

419 The time series of physical quantities measured at Argentière glacier over the 2017 and 2018
420 melt-season can be found at <https://doi.org/10.5281/zenodo.3701520>. All of the data associated
421 with the dense array experiment can be found at <https://doi.org/10.5281/zenodo.3971815>. The
422 spatial maps of source locations, glacier geometries and hydraulic potentials as well as the code
423 used to processed these data can be found at <https://doi.org/10.5281/zenodo.4024660>. Part of
424 the dataset of the seismic signals acquired during RESOLVE-Argentière can be found at
425 https://doi.org/10.15778/RESIF_ZO2018 in link with ref.³⁰. Contact U.N. at
426 ugo.nanni0158@gmail.com or ugo.nanni@univ-grenoble-alpes.fr for questions related to the
427 above described datasets and codes.

428

429

430 **References**

- 431 1. Shreve, R. L. Movement of Water in Glaciers. *J. Glaciol.* **11**, 205–214 (1972).
- 432 2. Iken, A. L. M. U. T., Truffer, M. & Truffe, M. The relationship between subglacial water
433 pressure and velocity of Findelengletscher, Switzerland, during its advance and retreat. *J.*
434 *Glaciol.* **43**, 328–338 (1997).
- 435 3. Davison, B. J., Sole, A. J., Livingstone, S. J., Cowton, T. R. & Nienow, P. W. The influence
436 of hydrology on the dynamics of land-terminating sectors of the Greenland ice sheet.
437 *Front. Earth Sci.* **7**, (2019).
- 438 4. Sole, A. J. *et al.* Seasonal speedup of a Greenland marine-terminating outlet glacier
439 forced by surface melt-induced changes in subglacial hydrology. *J. Geophys. Res. Earth*
440 *Surf.* **116**, 1–11 (2011).
- 441 5. Ritz, C. *et al.* Potential sea-level rise from Antarctic ice-sheet instability constrained by
442 observations. *Nature* **528**, 115–118 (2015).
- 443 6. King, M. D. *et al.* Dynamic ice loss from the Greenland Ice Sheet driven by sustained

- 444 glacier retreat. *Commun. Earth Environ.* **1**, 1–7 (2020).
- 445 7. Lliboutry, L. General Theory of Subglacial Cavitation and Sliding of Temperate Glaciers. *J.*
446 *Glaciol.* **7**, 21–58 (1968).
- 447 8. Röthlisberger, H. Water Pressure in Intra- and Subglacial Channels. *J. Glaciol.* **11**, 177–
448 203 (1972).
- 449 9. Kamb, B. Glacier surge mechanism based on linked cavity configuration of the basal
450 water conduit system. *J. Geophys. Res.* **92**, 9083 (1987).
- 451 10. Hubbard, B. P., Sharp, M. J., Willis, I., Nielsen, M. K. & Smart, C. C. Borehole water-level
452 variations and the structure of the subglacial hydrological system of Haut Glacier d' Arolla
453 ,. *J. Glaciol.* **41**, 572–583 (1995).
- 454 11. Schoof, C. Ice-sheet acceleration driven by melt supply variability. *Nature* **468**, 803–806
455 (2010).
- 456 12. Tedstone, A. J. *et al.* Decadal slowdown of a land-terminating sector of the Greenland Ice
457 Sheet despite warming. *Nature* **526**, 692–695 (2015).
- 458 13. Andrews, L. C. *et al.* Direct observations of evolving subglacial drainage beneath the
459 Greenland Ice Sheet. *Nature* **514**, 80–83 (2014).
- 460 14. Rada, C. & Schoof, C. Channelized, distributed, and disconnected: Subglacial drainage
461 under a valley glacier in the Yukon. *Cryosphere* **12**, 2609–2636 (2018).
- 462 15. Hoffman, M. J. *et al.* Greenland subglacial drainage evolution regulated by weakly
463 connected regions of the bed. *Nat. Commun.* **7**, 13903 (2016).
- 464 16. Sole, A. *et al.* Winter motion mediates dynamic response of the Greenland Ice Sheet to
465 warmer summers. *Geophys. Res. Lett.* **40**, 3940–3944 (2013).
- 466 17. Williams, J. J., Gourmelen, N. & Nienow, P. Dynamic response of the Greenland ice sheet

- 467 to recent cooling. *Sci. Rep.* **10**, 1–11 (2020).
- 468 18. Nienow, P., Sharp, M. & Willis, I. Seasonal changes in the morphology of the subglacial
469 drainage system, Haut Glacier d’Arolla, Switzerland. *Earth Surf. Process. Landforms* **23**,
470 825–843 (1998).
- 471 19. Tranter, M., Brown, G. H., Hodson, A. J. & Gurnell, A. M. Hydrochemistry as an indicator
472 of subglacial drainage system structure: a comparison of Alpine and Sub-Polar
473 environments. *Hydrol. Process.* **10**, 541–556 (1996).
- 474 20. Chandler, D. M. *et al.* Evolution of the subglacial drainage system beneath the Greenland
475 Ice Sheet revealed by tracers. *Nat. Geosci.* **6**, 195–198 (2013).
- 476 21. Bartholomäus, T. C., Amundson, J. M., Walter, J. I., O’Neel, S., West, M. E. & Larsen, C.
477 F. Subglacial discharge at tidewater glaciers revealed by seismic tremor. *Geophys. Res.*
478 *Lett.* **42**, 6391–6398 (2015).
- 479 22. Gimbert, F. *et al.* Subseasonal changes observed in subglacial channel pressure, size,
480 and sediment transport. *Geophys. Res. Lett.* **43**, 3786–3794 (2016).
- 481 23. Nanni, U. *et al.* Quantification of seasonal and diurnal dynamics of subglacial channels
482 using seismic observations on an Alpine glacier. *Cryosphere* **14**, 1475–1496 (2020).
- 483 24. Vore, M. E., Bartholomäus, T. C., Winberry, J. P., Walter, J. I. & Amundson, J. M. Seismic
484 Tremor Reveals Spatial Organization and Temporal Changes of Subglacial Water System.
485 *J. Geophys. Res. Earth Surf.* **124**, 427–446 (2019).
- 486 25. Lindner, F., Walter, F., Laske, G. & Gimbert, F. Glaciohydraulic seismic tremors on an
487 Alpine glacier. *Cryosphere* **14**, 287–308 (2020).
- 488 26. Burtin, A., Vergne, J., Rivera, L. & Dubernet, P. Location of river-induced seismic signal
489 from noise correlation functions. *Geophys. J. Int.* **182**, 1161–1173 (2010).

- 490 27. Rost, S. & Thomas, C. Array seismology: Methods and applications. *Rev. Geophys.* **40**, 2-
491 1-2-27 (2002).
- 492 28. Kuperman, W. A. & Turek, G. Matched field acoustics. *Mech. Syst. Signal Process.* **11**,
493 141–148 (1997).
- 494 29. Almendros, J., Ibáñez, J. M., Alguacil, G. & Del Pezzo, E. Array analysis using circular-
495 wave-front geometry: An application to locate the nearby seismo-volcanic source.
496 *Geophys. J. Int.* **136**, 159–170 (1999).
- 497 30. Gimbert, F. *et al.* A Multi-Physics Experiment with a Temporary Dense Seismic Array on
498 the Argentière Glacier, French Alps: The RESOLVE Project. *Seismol. Res. Lett.* (2021).
499 doi:10.1785/0220200280
- 500 31. Vincent, C. & Moreau, L. Sliding velocity fluctuations and subglacial hydrology over the
501 last two decades on Argentière glacier, Mont Blanc area. *J. Glaciol.* **62**, 805–815 (2016).
- 502 32. Sergeant, A. *et al.* On the Green's function emergence from interferometry of seismic
503 wave fields generated in high-melt glaciers: Implications for passive imaging and
504 monitoring. *Cryosphere* **14**, 1139–1171 (2020).
- 505 33. Legaz, A. *et al.* Self-potential and passive seismic monitoring of hydrothermal activity: A
506 case study at Iodine Pool, Waimangu geothermal valley, New Zealand. *J. Volcanol.*
507 *Geotherm. Res.* **179**, 11–18 (2009).
- 508 34. Chmiel, M., Roux, P. & Bardainne, T. High-sensitivity microseismic monitoring: Automatic
509 detection and localization of subsurface noise sources using matched-field processing and
510 dense patch arrays. *Geophysics* **84**, KS211–KS223 (2019).
- 511 35. Venkatesh, S. R., Polak, D. R. & Narayanan, S. Beamforming algorithm for distributed
512 source localization and its application to jet noise. *AIAA J.* **41**, 1238–1246 (2003).

- 513 36. Gimbert, F. *et al.* Seismological Research Letters The RESOLVE project : a multi-physics
514 experiment with a temporary dense seismic array on the Argentière Glacier , French Alps.
515 *Seismol. Res. Lett.* (2020).
- 516 37. Sergeant, A. *et al.* On the Green ' s function emergence from interferometry of seismic
517 wavefields generated in high-melt glaciers : implications for passive imaging and
518 monitoring. 1–52 (2019).
- 519 38. Aki, K. & Richards, P. G. *Quantitative seismology.* (University Science Books,U.S., 2002).
- 520 39. Lliboutry, L. Modifications to the theory of intraglacial waterways for the case of subglacial
521 ones. *J. Glaciol.* **29**, 216–226 (1983).
- 522 40. Kavanaugh, J. L. & Clarke, G. K. C. Abrupt glacier motion and reorganization of basal
523 shear stress following the establishment of a connected drainage system. *J. Glaciol.* **47**,
524 472–480 (2001).
- 525 41. Nienow, P. W., Sharp, M. & Willis, I. C. Velocity–discharge relationships derived from dye
526 tracer experiments in glacial meltwaters: implications for subglacial flow conditions.
527 *Hydrol. Process.* **10**, 1411–1426 (1996).
- 528 42. de Fleurian, B. *et al.* A modeling study of the effect of runoff variability on the effective
529 pressure beneath Russell Glacier, West Greenland. *J. Geophys. Res. F Earth Surf.* **121**,
530 1834–1848 (2016).
- 531 43. Gillet-Chaulet, F. *et al.* Assimilation of surface velocities acquired between 1996 and 2010
532 to constrain the form of the basal friction law under Pine Island Glacier. *Geophys. Res.*
533 *Lett.* **43**, 10,311–10,321 (2016).
- 534 44. Booth, A. D. *et al.* Distributed Acoustic Sensing (DAS) of Seismic Properties in a Borehole
535 drilled on a Fast-Flowing Greenlandic Outlet Glacier. *Geophys. Res. Lett.* 0–3 (2020).
536 doi:10.1002/ESSOAR.10502609.1

- 537 45. Soubestre, J. *et al.* Journal of Geophysical Research : Solid Earth Network-Based
538 Detection and Classification of Seismovolcanic Tremors : Example From the Klyuchevskoy
539 Volcanic Group in Kamchatka. (2018). doi:10.1002/2017JB014726
- 540 46. Moreau, L. *et al.* Sea Ice Thickness and Elastic Properties From the Analysis of
541 Multimodal Guided Wave Propagation Measured With a Passive Seismic Array. *J.*
542 *Geophys. Res. Ocean.* **125**, 1–17 (2020).
- 543 47. Irrazaval, I., Werder, M. A. & Huss, M. Determining the evolution of an alpine glacier
544 drainage system by solving inverse problems. 1–14 (2021).
- 545 48. Walter, F. *et al.* Distributed acoustic sensing of microseismic sources and wave
546 propagation in glaciated terrain. *Nat. Commun.* **11**, (2020).
- 547 49. Soubestre, J. *et al.* Depth Migration of Seismovolcanic Tremor Sources Below the
548 Klyuchevskoy Volcanic Group (Kamchatka) Determined From a Network-Based Analysis.
549 *Geophys. Res. Lett.* **46**, 8018–8030 (2019).
- 550 50. Mordret, A., Roux, P., Boué, P. & Ben-Zion, Y. Shallow three-dimensional structure of the
551 San Jacinto fault zone revealed from ambient noise imaging with a dense seismic array.
552 *Geophys. J. Int.* **216**, 896–905 (2019).
- 553 51. Bakker, M. *et al.* Field Application and Validation of a Seismic Bedload Transport Model.
554 *J. Geophys. Res. Earth Surf.* **125**, 0–3 (2020).
- 555 52. Vincent, C., Soruco, A., Six, D., Le Meur, E. & Meur, E. L. E. Glacier thickening and decay
556 analysis from 50 years of glaciological observations performed on Glacier d'Argentière,
557 Mont Blanc area, France. *Ann. Glaciol.* **50**, 73–79 (2009).
- 558 53. Hantz, D. & Lliboutry, L. Waterways, ice permeability at depth, and water pressures at
559 Glacier d'Argentiere, French Alps. *J. Glaciol.* **29**, 227–239 (1983).

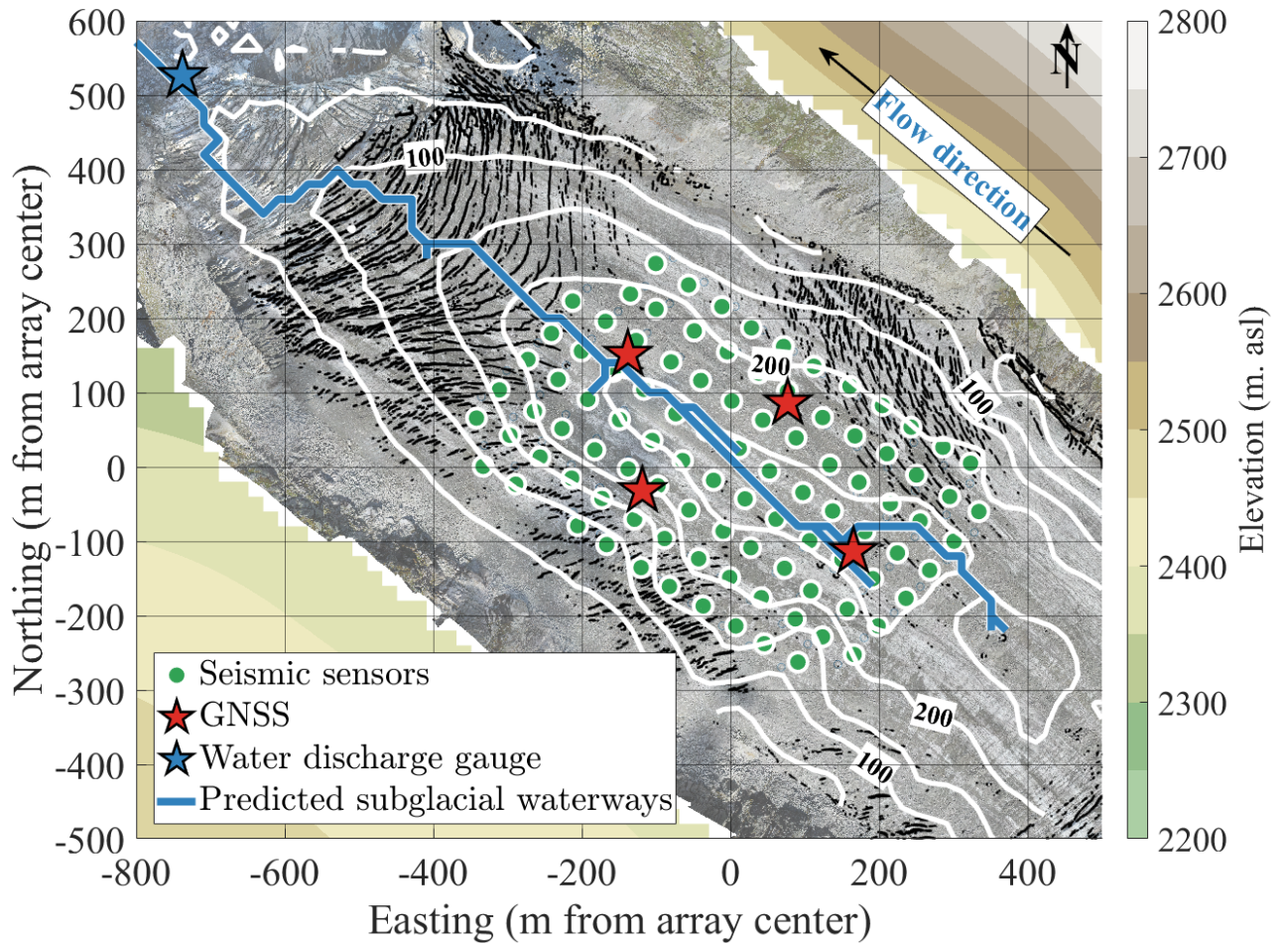
- 560 54. Nelder. Improved simplex method for function minimization. *Proceedings of the IEEE*
561 *International Conference on Systems, Man and Cybernetics* **3**, 1702–1705 (1996).
- 562 55. Chmiel, M., Roux, P. & Bardainne, T. Extraction of phase and group velocities from
563 ambient surface noise in a patch-array configuration. *Geophysics* **81**, KS231–KS240
564 (2016).
- 565 56. Pyrak-nolte, L. J., Mullenbach, B. L., Li, X., Nolte, D. D. & Grader, A. S. synthetic
566 sediments using seismic wave transmission Sample. *Geophys. Res. Lett.* **26**, 127–130
567 (1999).
- 568 57. Willis, I., Lawson, W., Owens, I., Jacobel, B. & Autridge, J. Subglacial drainage system
569 structure and morphology of Brewster Glacier, New Zealand. *Hydrol. Process. An Int. J.*
570 **23**, 384–396 (2009).
- 571 58. Schwanghart, W. & Scherler, D. Short Communication: TopoToolbox 2 - MATLAB-based
572 software for topographic analysis and modeling in Earth surface sciences. *Earth Surf.*
573 *Dyn.* **2**, 1–7 (2014).
- 574 59. De Fleurian, B. *et al.* A double continuum hydrological model for glacier applications.
575 *Cryosphere* **8**, 137–153 (2014).
- 576 60. Nye, J. F. The Flow of a Glacier in a Channel of Rectangular, Elliptic or Parabolic Cross-
577 Section. *J. Glaciol.* **5**, 661–690 (1965).
- 578 61. Hallet, B. The Effect of Subglacial Chemical Processes on Glacier Sliding. *J. Glaciol.* **17**,
579 209–221 (1976).
- 580
- 581

582

583 **Figures and Tables**

584

585 **Figure 1.**



586

587 Monitoring set-up of Glacier d'Argentière. Aerial view of the Glacier d'Argentière field site (France,

588 Mont Blanc mountain range) and location of the instruments used in this study. The seismic

589 network (green dots) is composed of 98 seismic stations with Fairfield Nodal Z-Land 3

590 components, which are indicated according to their positions at the beginning of the survey

591 period. Surface displacement was measured through four GNSS stations that functioned during

592 the study period (red stars). Subglacial water discharge (blue star) was measured through direct

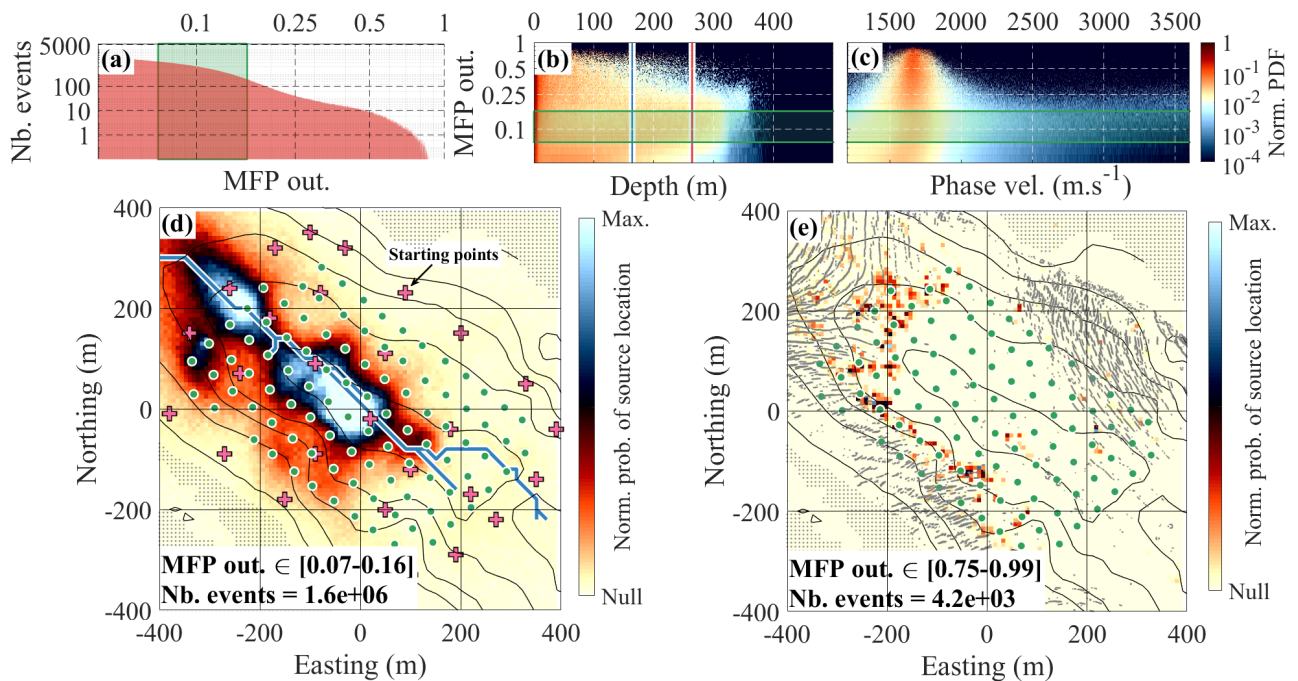
593 access to the glacier base from excavated tunnels. White contour lines show 50-m-spaced ice
594 thickness contours, as obtained from combined radar measurements and surface elevations. The
595 blue line shows the subglacial waterways as predicted from hydraulic potential calculations (see
596 Methods). The glacier flows toward the northwest (top left). Aerial view provided by Bruno
597 Jourdain.

598

599

600

601 **Figure 2.**



602

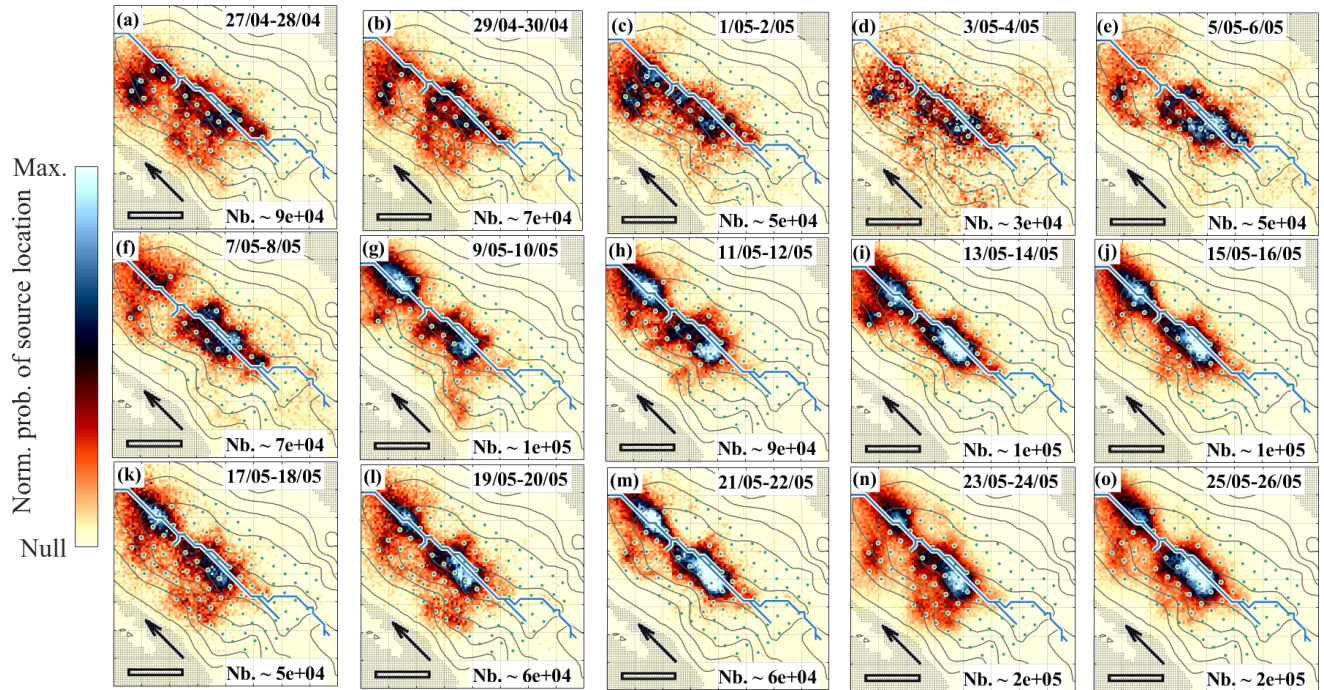
603 Statistics and two-dimensional representation of the matched-field processing (MFP) output for
604 the 5 ± 2 Hz frequency range. (a) Distribution of the average number of events located per day
605 after applying the selection as a function of the MFP output. Green shaded area shows the [0.07-
606 0.16] MFP output range for which the spatial distribution of the sources was investigated. (b)
607 Normalized probability distribution of the MFP output as a function of source depth relative to the
608 surface. The vertical red line shows the maximum ice thickness; the blue line shows the median
609 ice thickness. The green shaded areas show the [0.07-0.16] MFP output range. (c) Normalized
610 probability distribution of the MFP output as a function of the phase velocity. Note that the color
611 scales are logarithmic and the distribution is normalized per MFP output band of 0.01. The green
612 shaded areas show the [0.07-0.16] MFP output range. (d, e) Two-dimensional representation of
613 the normalized probability of the source location obtained with 8 × 8 m² pixels grid for the study
614 area for the two MFP output ranges [0.07-0.16] (d) and [0.75-0.99] (e). Contour lines show 50-m-

615 spaced ice thickness contours, as shown in Figure 1. The gray shading shows ice-free areas. The
616 green dots show the seismic array. The blue line in (d) shows the subglacial waterways as
617 predicted from the hydraulic potential calculation, as shown in Figure 1. The black dots in (e)
618 show crevasse locations, as shown in Figure 1. The pink crosses in (d) show the locations of the
619 29 starting points used in the location algorithm.

620

621 **Figure 3.**

622



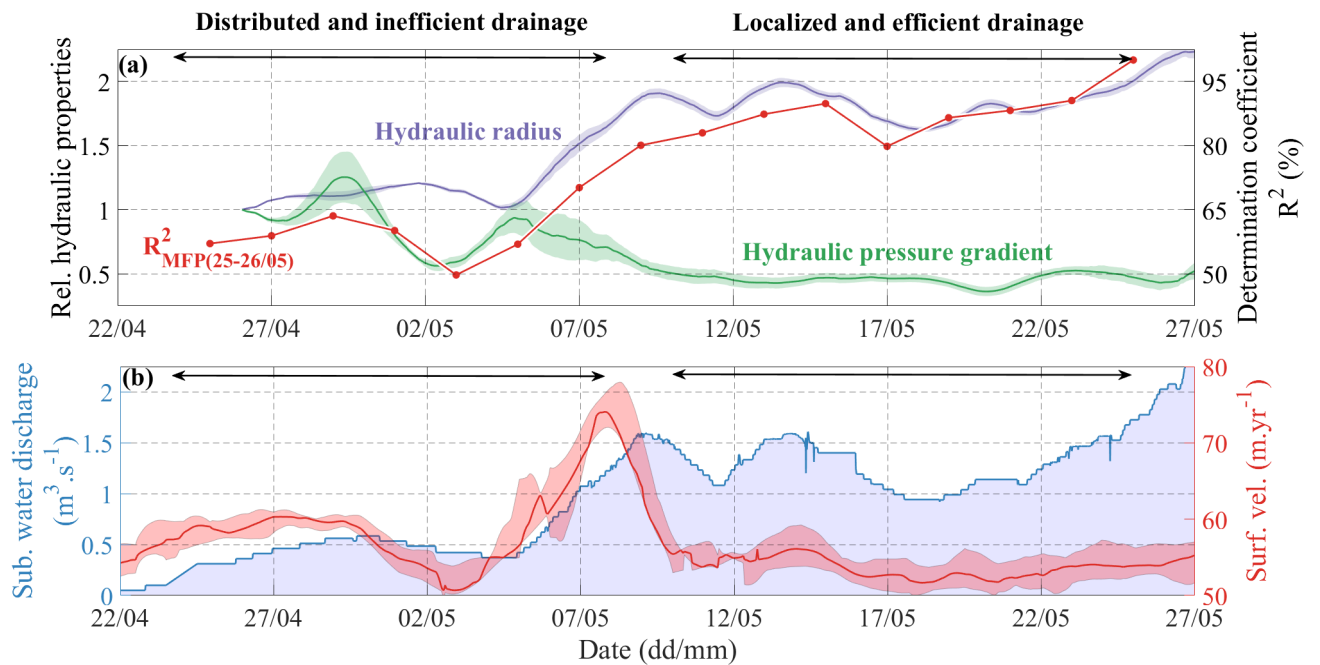
623

624 Two-dimensional maps of subglacial water flow source location obtained from matched-field
625 processing (MFP). Temporal evolution of the spatial patterns of the source location densities
626 obtained for the 5 ± 2 Hz frequency range and the [0.07-0.16] MFP output range. All of the maps
627 are averaged over 2-day time windows, with the associated number of the sources located shown
628 in the bottom right corner (Nb.). Color scale ranges are normalized for each time window using
629 maximum probability. (o) The characteristic pattern used in Figure 4 for calculation of the
630 coefficient of determination. Contour lines show the 50-m-spaced ice thickness contours, as
631 shown in Figure 1. The gray shading shows ice-free areas. Scale bars (bottom left): 200 m. The
632 blue lines show the subglacial waterways, as predicted from the hydraulic potential calculation,
633 and as shown in Figure 1. Black arrows show glacier and subglacial water flow directions.

634

636 **Figure 4.**

637



638

639 Temporal evolution of the subglacial hydraulic properties, seismic observations, and glacier flow.

640 (a) Left axis shows the relative hydraulic properties, as averaged over the 98 sensors. Hydraulic
641 pressure gradient with ± 1 median absolute deviation (MAD), as the shaded envelope (green), and

642 hydraulic radius with ± 1 MAD, as the shaded envelope (purple). Both values are expressed as

643 relative to April 26. Right axis shows temporal evolution of the spatialized seismic observations

644 using the determination coefficient R^2 of the source location pattern shown in Figure 3o (red).

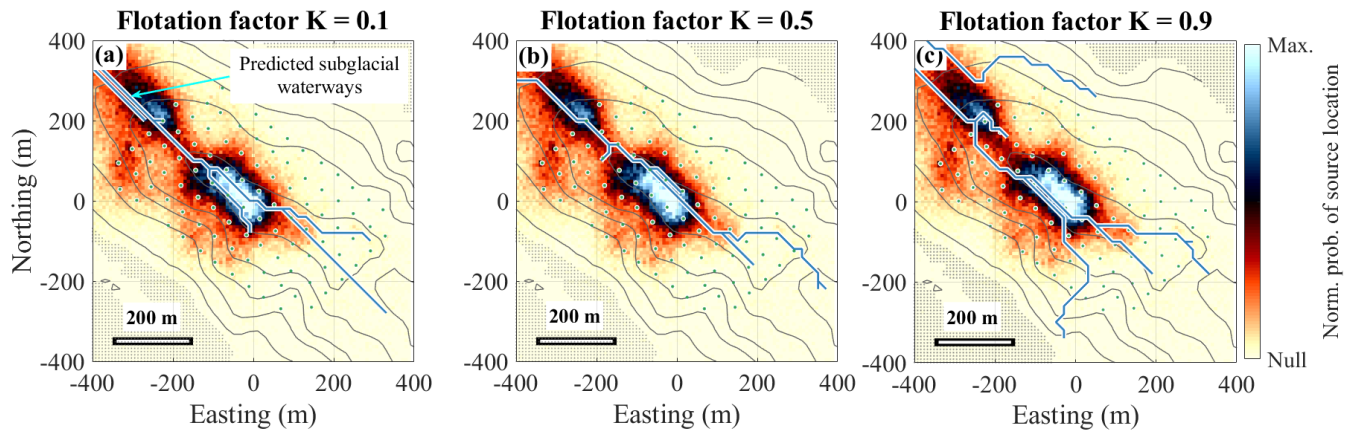
645 The closer this coefficient is to 1, the more the drainage system is observed to be channelized.

646 (b) Subglacial water discharge (blue line) with shaded blue area under the curve added for ease

647 of reading. Median surface velocity over the four on-ice GNSS stations (red line) with the

648 minimum/maximum shaded envelope.

649 **Supplementary Figure 1.**



650

651 Two-dimensional representation of the normalized probability of the source location obtained with
 652 8×8 m² pixels grid for the study area for the two MFP output ranges [0.07-0.16] as shown in Fig.
 653 2d. The blue line shows the subglacial waterways as predicted from hydraulic potential
 654 calculations for three different values of flotation fraction K (see Methods for details). Green dots
 655 show seismic sensors location.